Towards identifying the active sites on RuO2(110) in catalyzing oxygen evolution

Rao, Reshma R. ; Kolb, Manuel J. ; Halck, Niels Bendtsen; Pedersen, Anders Filsøe; Mehta, Apurva; You, Hoydoo ; Stoerzinger, Kelsey A. ; Feng, Zhenxing ; Hansen, Heine Anton; Zhou, Hua

Total number of authors:
16

Published in:
Energy & Environmental Science

Link to article, DOI:
10.1039/c7ee02307c

Publication date:
2017

Document Version
Peer reviewed version

Towards identifying the active sites on RuO_2(110) in catalyzing oxygen evolution†

Reshma R. Rao, [a] Manuel J. Kolb, ‡[b] Niels Bendtsen Halck,[c] Anders Filsøe Pedersen, [d] Apurva Mehta,[e] Hoydoo You,[f] Kelsey A. Stoerzinger,§[g] Zhenxing Feng, [h] Heine A. Hansen,[c] Hua Zhou,[i] Livia Giordano,[aj] Jan Rossmeisl,[k] Tejs Vegge, [c] Ib Chorkendorff, [d] Ifan E. L. Stephens¶[d] and Yang Shao-Horn *[abg]

Received 14th August 2017,
Accepted 17th November 2017

While the surface atomic structure of RuO_2 has been well studied in ultra high vacuum, much less is known about the interaction between water and RuO_2 in aqueous solution. In this work, *in situ* surface X-ray scattering measurements combined with density functional theory (DFT) were used to determine the surface structural changes on single-crystal RuO_2(110) as a function of potential in acidic electrolyte. The redox peaks at 0.7, 1.1 and 1.4 V *vs.* reversible hydrogen electrode (RHE) could be attributed to surface transitions associated with the successive deprotonation of $-H_2O$ on the coordinatively unsaturated Ru sites (CUS) and hydrogen adsorbed to the bridging oxygen sites. At potentials relevant to the oxygen evolution reaction (OER), an –OO species on the Ru CUS sites was detected, which was stabilized by a neighboring –OH group on the Ru CUS or bridge site. Combining potential-dependent surface structures with their energetics from DFT led to a new OER pathway, where the deprotonation of the –OH group used to stabilize –OO was found to be rate-limiting.

Broader context

Storing electrical energy in chemical bonds by splitting water is an effective way to distribute clean energy from solar and wind. Generation of molecular oxygen is the most energy intensive part of the process, limiting the overall efficiency of water splitting devices. RuO_2 is a gold standard catalyst for these devices, with record activities for the oxygen evolution reaction (OER). Additionally, it can undergo fast surface redox reactions in the electrochemically stable potential window of water, making it a model material for electrochemical capacitors that can charge and discharge in a much shorter time scale than batteries. Understanding the interaction of RuO_2 with water can provide critical insights into the physical origin of its fascinating electrochemical properties and the active site(s) for catalytic reactions in aqueous solution. Our work reveals how single-crystal RuO_2(110) interacts with water to generate different oxygenated adsorbed species as a function of potential. We propose an OER-active surface where the final proton release from a stabilized –OOH configuration is rate limiting. These findings provide new mechanistic insights into the origin of the redox transitions, and active sites for OER, and opportunities to enhance the capacitance and catalytic activity for the OER.

[a] *Department of Mechanical Engineering, Massachusetts Institute of Technology, Cambridge, Massachusetts 02139, USA. E-mail: shaohorn@mit.edu*
[b] *Research Laboratory of Electronics, Massachusetts Institute of Technology, Cambridge, Massachusetts 02139, USA*
[c] *Department of Energy Conversion and Storage, Technical University of Denmark, 2800 Kgs. Lyngby, Denmark*
[d] *Section for Surface Physics and Catalysis, Department of Physics, Technical University of Denmark, 2800 Kgs. Lyngby, Denmark*
[e] *SLAC National Accelerator Laboratory, Menlo Park, CA 94025, USA*
[f] *Argonne National Laboratory, Materials Science Division, Argonne, Illinois 6043, USA*
[g] *Department of Materials Science and Engineering, Massachusetts Institute of Technology, Cambridge, Massachusetts 02139, USA*
[h] *School of Chemical, Biological, and Environmental Engineering, Oregon State University, Corvallis, OR 97331, USA*
[i] *X-ray Science Division, Argonne National Laboratory, Argonne, IL 60439, USA*
[j] *Dipartimento di Scienza dei Materiali, Università di Milano-Bicocca, Milano, Italy*
[k] *Department of Chemistry, University of Copenhagen, Universitetsparken 5, 2100 Copenhagen, Denmark*

† Electronic supplementary information (ESI) available. See DOI: 10.1039/c7ee02307c

‡ Current address: FYSIKUM, AlbaNova, Stockholm University, S-10691 Stockholm, Sweden and SUNCAT Center for Interface Science and Catalysis, Department of Chemical Engineering, Stanford University, 443 *Via* Ortega, Stanford, California 94305, USA.
§ Current address: Physical and Computational Sciences Directorate, Pacific Northwest National Laboratory, Richland, Washington 99354, USA.
¶ Current address: Royal School of Mines, Imperial College London, South Kensington Campus, London, SW 2AZ, UK.

Introduction

Rutile RuO_2 has record activity for catalyzing the oxygen evolution reaction (OER) upon water splitting,[1–8] the slow kinetics of which hamper the efficiency of hydrogen production.[9–16] In addition, RuO_2 exhibits high pseudocapacitance in aqueous electrolytes,[17–19] making it a benchmark material for electrochemical capacitors.[20–23] Understanding the interaction between water and RuO_2 surfaces as a function of potential is needed to understand the physical origin of the high OER activity and high pseudocapacitance of rutile RuO_2.

Much of our current understanding of RuO_2 surface structures and reactivity comes from ultra high vacuum (UHV) and density functional theory (DFT) studies as it is used as a model system to catalyze chlorine evolution (HCl oxidation),[24,25] CO oxidation,[26–29] methanol oxidation,[30] NH_3 oxidation,[31] and NO oxidation.[32] The rutile (110) surface is the most well studied, which can consist of two different Ru sites – a coordinatively unsaturated site (CUS) uncapped by oxygen and bound to five O atoms, and a bridge site (BRI) bound to six O atoms.[24–30,33–39] Over *et al.* have shown using scanning tunneling microscopy (STM) that the stoichiometric $RuO_2(110)$ termination has the bridge Ru filled with oxygen but the CUS Ru unfilled.[26] Further exposure to oxygen at room temperature resulted in the adsorption of oxygen species on CUS Ru,[27,28,30] which is supported by X-ray photoelectron spectroscopy coupled with DFT calculations.[29,33,34] Therefore, CUS Ru has been considered as the active site for catalyzing oxidation of small molecules.[4,40]

While some studies have examined the interactions between water and rutile RuO_2 surfaces using DFT[36] and STM,[41,42] the interaction of RuO_2 with water is poorly understood. DFT studies of $RuO_2(110)$ have shown that exposure to low partial pressure of water vapor leads to the formation of one hydroxyl group per unit cell, on either the bridge (OH_{BRI}/O_{CUS}) or CUS (O_{BRI}/OH_{CUS}) site. Exposure to high partial pressure of water results in chemisorbed water on CUS Ru (O_{BRI}/H_2O_{CUS}) or hydroxylation of both CUS and bridge Ru sites (OH_{BRI}/OH_{CUS}),[36] where the presence of chemisorbed water on CUS Ru sites is supported by high-resolution electron energy loss spectroscopy (HREELS).[35] In addition, recent STM studies coupled with DFT calculations[41,42] suggest that water clusters are stabilized by donating one proton per every two water molecules to the bridge oxygen, and provide experimental evidence for these two energetically degenerate structures (O_{BRI}/H_2O_{CUS} and OH_{BRI}/OH_{CUS}) predicted at high water pressures.[36]

Much less is known about the surface atomic structure changes on $RuO_2(110)$ as a function of potential prior to the OER, and the surface atomic structure and chemistry of $RuO_2(110)$ at OER-relevant potentials. Such information can provide key insights for identifying the configuration and chemistry of the active sites, understanding how they energetically interact with OER intermediates and revealing the OER mechanism. The conventional OER mechanism proposed on oxide surfaces such as $RuO_2(110)$ from DFT studies involves four proton coupled electron transfer steps where a water molecule is adsorbed on the CUS Ru site and deprotonated to form an –OH and –O consecutively. A second water molecule dissociates on the –O bound to the CUS Ru forming –OOH which undergoes the final deprotonation step that results in the evolution of oxygen. The formation of –OOH from –O is considered rate limiting in the conventional OER mechanism.[37,39,43] This OER mechanism proposed on $RuO_2(110)$ implies that the surface relevant to OER should be oxidized, having both CUS and bridge Ru sites filled with oxygen since the –OOH to O_2 step is energetically downhill in free energy at OER relevant potentials. This mechanism is challenged by recent DFT studies on $IrO_2(110)$, which show that a stable –OOH-like configuration can be realized on the surface, where the –OOH can transform to an –OO species bound to the CUS Ir site without a barrier, which is stabilized by an –OH bound to a neighboring Ir.[44] While the proposed rate limiting step in this previous study is still the formation of –OOH from –O, the free energy for steps from –O to –OOH and from –OOH to $O_2(g)$ is comparable due to the stabilized –OOH, potentially suggesting a different surface structure at OER potentials from the conventional mechanism.[44] However, there is no experimental evidence that supports either proposed surface structure at OER-relevant potentials.

Understanding surface structure changes responsible for experimentally observed redox potentials prior to OER can provide insights into what governs the OER activity. In the conventional mechanism, the OER activity descriptor, $\Delta G_{O_{ad}} - \Delta G_{OH_{ad}}$ from DFT studies,[37,43] can be related directly to the redox potentials of metal oxides prior to OER. For example, the free energy of the proton-coupled electron transfer step, $[M^{n+}\text{–}OH] \rightarrow [M^{n+1}\text{–}O] + H^+ + e^-$ in acid or $[M^{n+}\text{–}OH] + OH^- \rightarrow [M^{n+1}\text{–}O] + H_2O + e^-$ in alkaline solution, can be expressed as $\Delta G_n = \Delta G_{O_{ad}} - \Delta G_{OH_{ad}} - eV_{RHE}$, where $\Delta G_{O_{ad}}$ and $\Delta G_{OH_{ad}}$ are the free energies of adsorption of O_{ad} (M^{n+1}–O_{ad}) and OH_{ad} (M^{n+}–OH_{ad}), respectively. Therefore, the redox potential corresponding to the $[M^{n+}\text{–}OH_{ad}]/[M^{n+1}\text{–}O_{ad}]$ transition prior to OER, eV_{RHE}, directly equates to the activity descriptor, $\Delta G_{O_{ad}} - \Delta G_{OH_{ad}}$. Kuo *et al.*,[49] have first used this approach to correlate OER activity at different pH with estimated $\Delta G_{O_{ad}} - \Delta G_{OH_{ad}}$ from the redox potential ($\sim$1.5 V_{RHE} at pH 13) observed on the $IrO_2(110)$ surface. In addition, our previous work has shown that the charge associated with the redox peak at $\sim$1.4 V_{RHE} for different surfaces of oriented RuO_2 films increases with the OER activity, suggesting that this redox peak prior to the OER generates active sites catalyzing the OER.[5,46,47] Unfortunately, connecting reported computed surface structure changes with experimentally observed redox peaks is not straightforward as the computed and experimental potentials can differ greatly. DFT calculations show that Ru CUS sites on $RuO_2(110)$ are filled with –OH at $\sim$0.6 V_{RHE} while hydroxylated bridge Ru sites become deprotonated at $\sim$1.0 V_{RHE}.[45] On the other hand, experimentally, $RuO_2(110)$ exhibits redox reactions at $\sim$1.0 and $\sim$1.3 V_{RHE} in base[5,46,47] and $\sim$0.7, $\sim$1.1 and $\sim$1.4 V_{RHE} in acid prior to the OER,[48] which can be attributed to successive deprotonation/oxidation of adsorbates bound to Ru sites.[17–19] In addition, adsorption of –OH and –O at the Ir CUS site based on the DFT results occurs at $\sim$0.9 and $\sim$1.3 V_{RHE}, which correlates well with the first redox transition at 0.9 V_{RHE}, but differs significantly from the second redox transition at 1.5 V_{RHE}.[49]

In this study, we employ surface X-ray scattering, or crystal truncation rod (CTR) analysis to measure the atomic structure changes of single crystal RuO_2(110) *in situ* as a function of potential in acid, which is complemented by DFT studies. CTR has been used to study surface structure changes of metal and oxide surfaces such as Au,[50,51] Pt[51,52] and Ag,[53] and rutile RuO_2[38,48,54,55] and TiO_2[56,57] interfacing with water. Previous CTR measurements of RuO_2(110) in base[38] have reported the filling of the CUS Ru sites at $\sim$0.8 V_{RHE}, while the bridge site is unfilled.[38] However, such findings are contradictory to surface science[26–28,30] and DFT studies,[36,45] which show that the bridge Ru is filled with –O, –OH or –H_2O before or simultaneously with CUS Ru. In this work, we use DFT to compute energetics of surface adsorbates and assist the refinement of atomic structures from CTR measurements. Using this synergistic approach, we find that while the bridge oxygen atoms are protonated at potentials as low as 0.5 V_{RHE}, water dissociation is observed at the CUS site at 1.0 V_{RHE}. At these potentials, every second water molecule dissociates to form an –OH group, while only every second bridging oxygen site is protonated. The redox transition at $\sim$1.1 V_{RHE} results in a completely hydroxylated CUS site. More notably, we experimentally find that a –OO like species is stable just prior to oxygen evolution at 1.5 V_{RHE}. This is supported by our DFT calculations that suggest that the structure formed by the barrierless transfer of hydrogen from an –OOH structure to the neighboring oxygen is stable in this potential region due to the strong interaction between the –OO and neighboring –OH group. Our work provides unique experimental evidence of the OER active surface for RuO_2(110) and proposes different OER reaction steps from the conventional OER mechanism.

Results and discussion

Synchrotron X-ray scattering measurements were performed on a single crystal RuO_2(110) surface at 0.5, 1.0, 1.3 and 1.5 V_{RHE} in 0.1 M $HClO_4$ using a three-electrode cell (Fig. 1A, C and Fig. S1, ESI†). Specular and off-specular reflectivity data collected *in situ* allowed the determination of structural changes associated with three distinct redox processes centered at $\sim$0.7, $\sim$1.1 and $\sim$1.4 V_{RHE} prior to the OER, as shown in Fig. 1A (Fig. S1, ESI†).

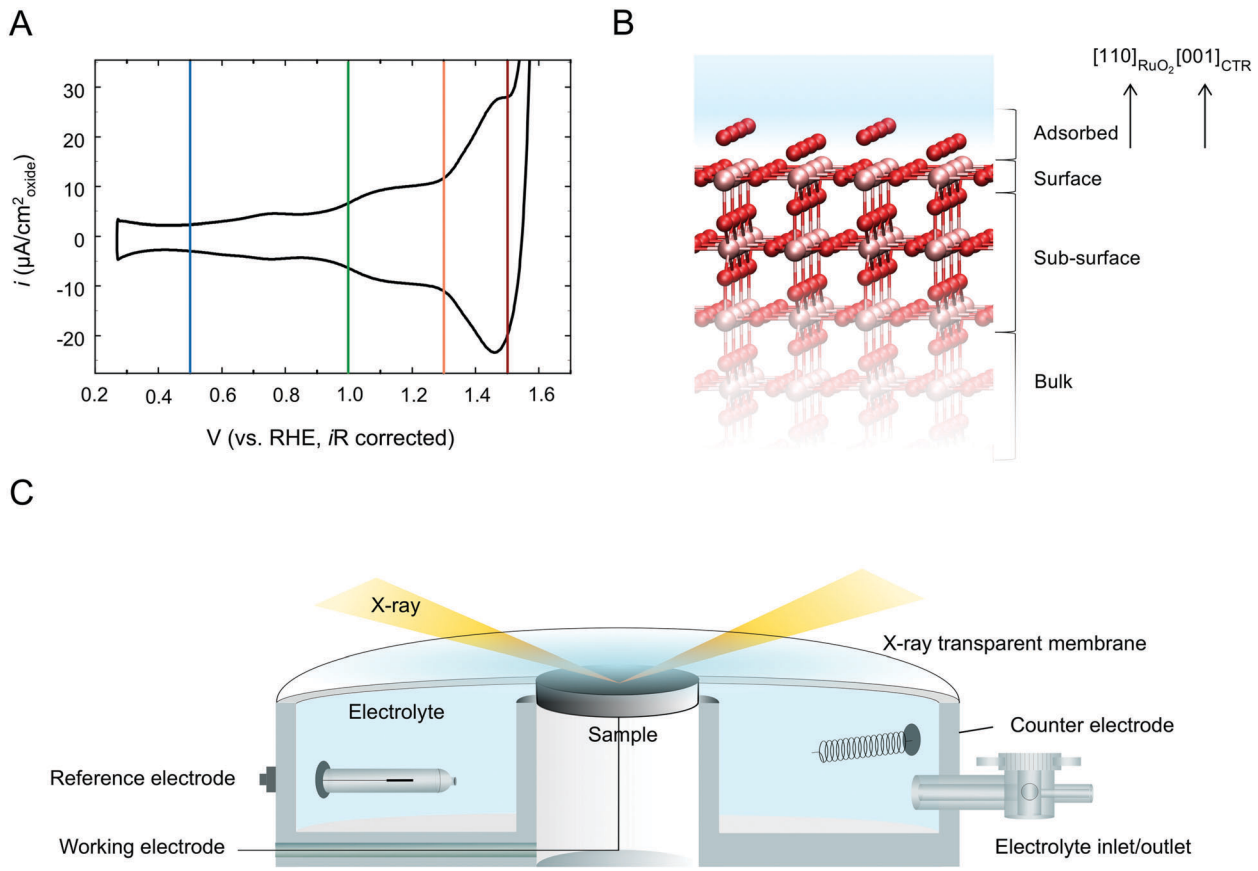

Fig. 1 (A) Cyclic voltammogram of a RuO_2(110) single crystal surface in Ar-saturated 0.1 M $HClO_4$ solution ($\sim$pH 1.2) measured at a scan rate of 50 mV s^{-1}. The vertical lines at 0.5 V, 1.0 V, 1.3 V and 1.5 V_{RHE} indicate the potentials at which surface diffraction measurements were performed. (B) Model of the (110) surface used for fitting. Pink and red spheres represent Ru and O atoms respectively. All atoms in the 'adsorbed', 'surface' and 'sub-surface layer' were allowed to relax in the *z* direction, with the constraints being tighter for the 'sub-surface' layer atoms. The lattice parameters in the *z* direction for the 'bulk' and 'sub-surface' layer were also allowed to relax (detailed atomic positions and fitting parameters are included in Fig. S4 and Table S1 ESI†). (C) Schematic of the three-electrode X-ray electrochemical cell and the X-ray scattering geometry.

Six unique truncation rods were measured, namely, (01L), (10L), (00L), (11L), (02L) and (20L). Plane normal to $(001)_{RuO_2}$ and $(1{-}10)_{RuO_2}$ which are in plane, and plane normal to $(110)_{RuO_2}$ are referred to as plane normal to (100), (010) and (001) in the CTR measurements, respectively. Since the symmetry of $(110)_{RuO_2}$ or $(00L)_{CTR}$ gives rise to the fact that the intensity of (01L) and (10L) rods (with $h + k$ values odd) comes predominantly from oxygen atoms, making these rods sensitive to changes in surface adsorbed oxygen species, they are referred to as 'oxygen rods' (see ESI† for more details).

The measured intensity (in open circles) of (01L), (10L) and (00L) rods at 0.5, 1.0, 1.3 and 1.5 V_{RHE} is shown in Fig. 2. The (00L) (Fig. 2), (02L), (11L) and (20L) rods (Fig. S5, ESI†) remained unchanged largely as a function of potential. As the intensity of these rods is predominately dependent on Ru atom position, we can conclude that the position of surface Ru did not change

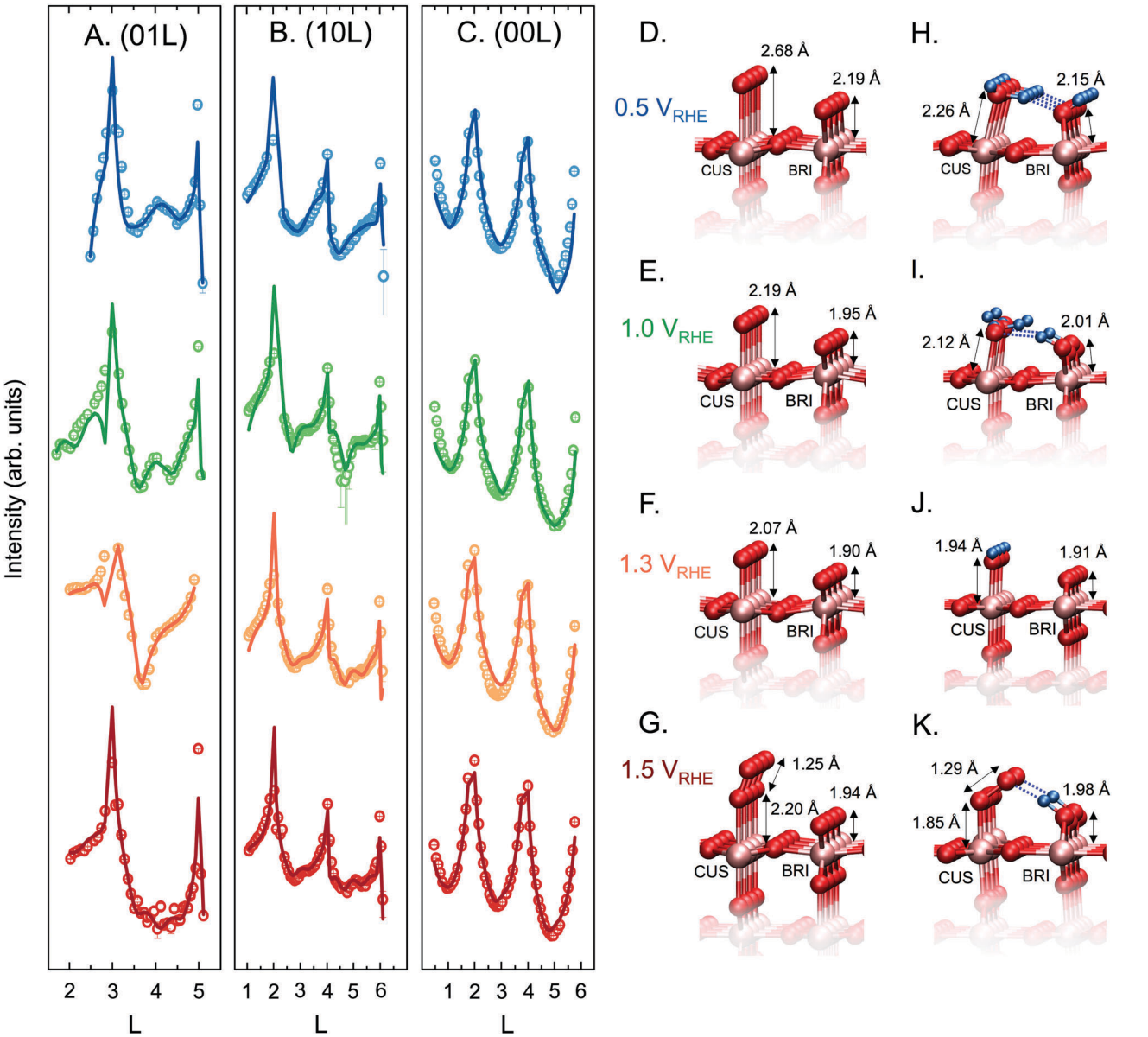

Fig. 2 (A) (01L) (B) (10L) and (C) (00L) rods measured at the four different potentials, 0.5 V_{RHE}, 1.0 V_{RHE}, 1.3 V_{RHE} and 1.5 V_{RHE} as indicated. The experimentally measured intensities are shown as open points and the best-fit results from the fitting process are shown as solid lines of the corresponding color. Ball and stick models for the best-fit structures obtained for the (D) 0.5 V_{RHE}, (E) 1.0 V_{RHE}, (F) 1.3 V_{RHE} and (G) 1.5 V_{RHE} crystal truncation rod data. Maximum experimental uncertainty in bond lengths is 0.06 Å, with detailed uncertainty of each bond length shown in Fig. S12 (ESI†). Most stable adsorbate configuration obtained from DFT calculations at (H) 0.5 V_{RHE} and (I) 1.0 V_{RHE}. The Ru_{CUS}–O bond length is the average value of the Ru_{CUS}–H_2O (2.17 Å) and Ru_{CUS}–OH (2.07) Å and the Ru_{BRI}–O bond length is an average value of the Ru_{BRI}–OH (2.10 Å) and Ru_{BRI}–O (1.92 Å) at (J) 1.3 V_{RHE} and (K) 1.5 V_{RHE}. The Ru_{CUS}–O bond length is the average value of the Ru_{CUS}–O (1.73 Å) and Ru_{CUS}–OO (1.96) Å and the Ru_{BRI}–O bond length is an average value of the Ru_{BRI}–OH (2.07 Å) and Ru_{BRI}–O (1.89 Å). Another degenerate structure was predicted by DFT at this potential, as shown in Fig. 3, with the CUS site occupied with an alternating –OO (Ru_{CUS}–OO = 1.88 Å) and –OH (Ru_{CUS}–OH = 1.95 Å) and the bridge site occupied with a –O group (Ru_{BRI}–O = 1.92 Å). Pink, red and blue spheres represent Ru, O and H atoms respectively. Bond lengths between surface Ru and adsorbed O species are labeled.

significantly with increasing potential. In contrast, the (01L) and (10L) rods underwent marked changes at the anti-Bragg positions, regions of low intensity, between two adjacent Bragg peaks, which indicated considerable changes of surface adsorbates as a function of potential. These spectra were fitted to a surface structure model that consists of Ru and O shown in Fig. 1B using GenX[58] (see Fig. S6–S11, ESI† for sensitivity of fit analysis), which includes one 'adsorbed' layer and RuO_2 'surface', 'subsurface' and 'bulk' layers. As the technique is insensitive to the presence of hydrogen atoms (due to the low scattering power of hydrogen), hydrogen atoms were not considered for the 'adsorbed' layer. Interpretations about the nature of the oxy-species as a function of potential were made by comparing the fitted bond lengths to literature values of Ru–O bond lengths for $-H_2O$, –OH and –O. DFT was used to examine the energetics of the surface structure as a function of potential in order to assist the fitting of CTR data and increase confidence in the fitted structures, as shown in Fig. 3. Several different adsorption configurations were tested based on the experimental CTR results and the most stable structure realized at a given potential is the one with the lowest Gibbs adsorption energy at that potential.

Surface structure at 0.5 V_{RHE}

At 0.5 V_{RHE}, the fitting of all six rods yielded a surface structure with the presence of oxygen on both the CUS and bridge sites

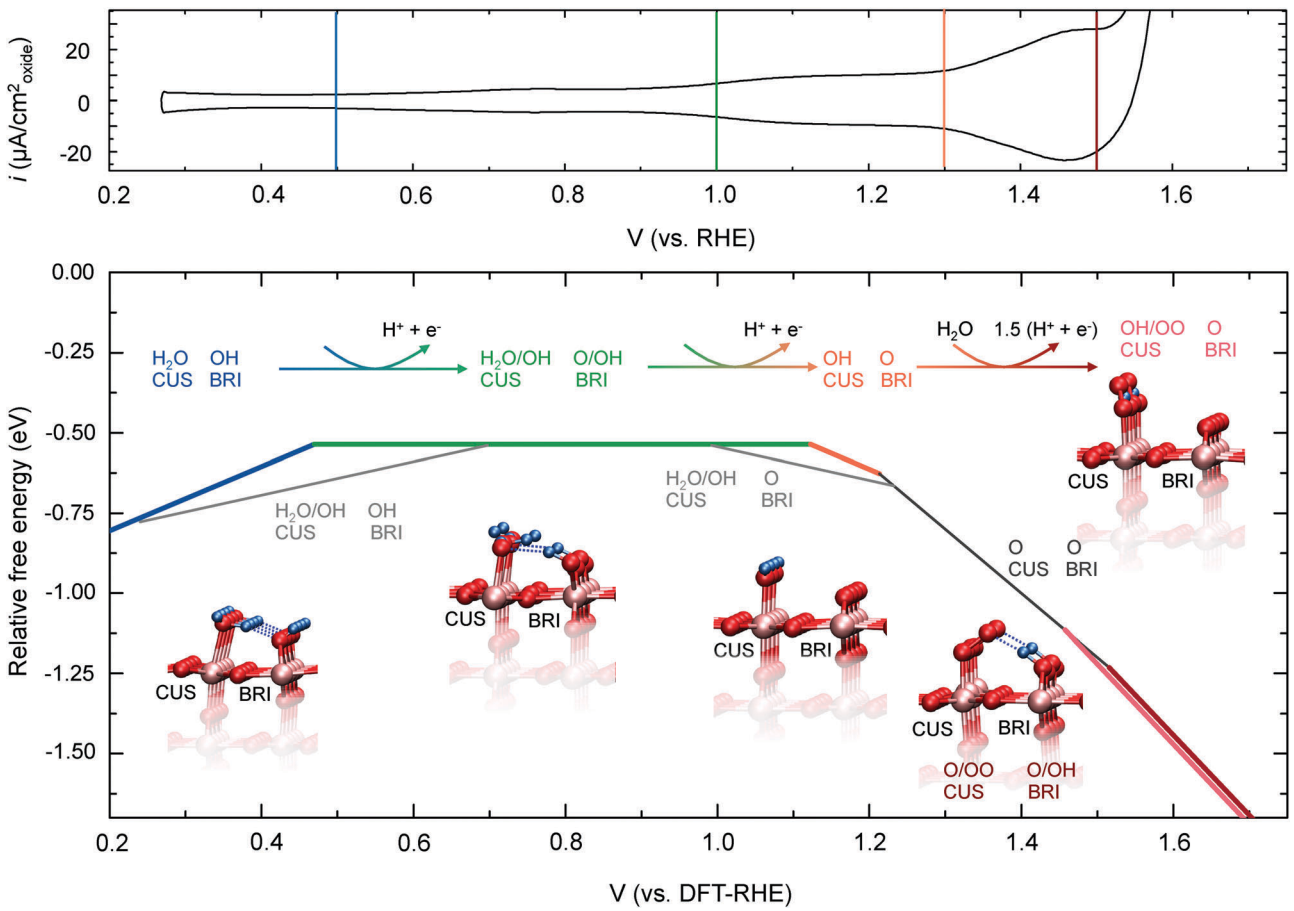

Fig. 3 (top) Reference cyclic voltammogram of a RuO_2(110) single crystal surface in Ar-saturated 0.1 M $HClO_4$ solution (~pH 1.2) measured at a scan rate of 50 mV s^{-1}. The vertical lines at 0.5 V, 1.0 V, 1.3 V and 1.5 V_{RHE} indicate the potentials at which surface diffraction measurements were performed. (bottom) DFT-generated diagram showing the relative Gibbs adsorption energies of the most stable adsorbate configurations at different applied electrochemical potential. The structure realized at a specific potential is the one with the lowest free energy at that potential, and the transition from one stable structure to another (depicted by the intersection point of two lines) corresponds to an experimentally observed redox transition. The *x*-axis for the top and bottom figure shows the applied potential of the cyclic voltammogram trace (black) and the calculated DFT potential *vs.* RHE ($V_{DFT-RHE}$) respectively. The most stable facets at each voltage are shown in thick lines, with the configuration corresponding to the lines noted. Grey lines indicate stable terminations in DFT that were not accessed in the experimental measurements. The first redox transition at ~0.7 V_{RHE} results in the loss of 0.5 ($H^+ + e^-$) per CUS Ru to form –OH from $-H_2O$ on every alternate site, and a loss of 0.5 ($H^+ + e^-$) per bridging oxygen to form a structure where only every alternate bridging oxygen has a hydrogen adsorbed to it. The second redox transition at ~1.1 V_{RHE} results in the water on alternate CUS Ru forming an –OH (0.5 ($H^+ + e^-$)/Ru_{CUS}) and the removal of the remaining hydrogen adsorbed to bridging oxygens (0.5 ($H^+ + e^-$)/Ru_{BRI}). The final redox transition first leads to the CUS site getting fully oxidized (1 ($H^+ + e^-$)/Ru_{CUS}) and then water dissociating on every alternate CUS Ru followed by a chemical transformation to form a stabilized –OOH configuration ((0.5 ($H^+ + e^-$)/Ru_{CUS})). Ball and stick models of the configurations predicted at the experimental potentials of 0.5 V_{RHE}, 1.0 V_{RHE}, 1.3 V_{RHE} and 1.5 V_{RHE} are shown. Pink, red and blue spheres represent Ru, O and H atoms respectively. Hydrogen bonds are drawn with blue dashed lines where applicable.

but with considerably different bond lengths (Fig. 2D). As the Ru_{CUS}–O bond length (2.68(3) Å) was significantly larger than the apical Ru–O bond length (1.94 Å)[4] in rutile RuO_2, and that for adsorbed O on Ru CUS sites (1.70 Å),[34] this oxygen species is assigned as loosely bound water on the CUS site. On the other hand, the fitted Ru_{BRI}–O bond length is 2.19(4) Å, which is longer than the apical Ru–O (1.94 Å)[4] bond length in rutile RuO_2 and Ru_{BRI}–O bond length (1.93 Å) on the stoichiometric surface from previous LEED measurements.[26] Therefore, we assign this to protonated bridging oxygen species. Such assignments are different from previous CTR measurements of RuO_2(110) surfaces in alkaline media, which report that the CUS site is filled with –OH having a bond length of 2.23(2) Å[38] while the bridge Ru site is empty. Our assignment is supported by detailed sensitivity of fit analysis (Fig. S6, ESI†), which explicitly shows that the bridge Ru site is filled prior to the CUS site, in accordance with previous surface science[26–28,30] and DFT results.[36,45] Further evidence for this surface structure fitted from CTR measurements at 0.5 V_{RHE} (Fig. 2D and Fig. S12A, ESI†) came from our DFT studies, which show that the filling of CUS sites by $-H_2O$ (with greater Ru_{CUS}–O distance of 2.26 Å) and protonation of bridging oxygen (with shorter Ru_{BRI}–O distance of 2.15 Å) occurs with increasing voltage up to $\sim$0.5 $V_{DFT-RHE}$ in the DFT RHE scale (Fig. 2H and Fig. 3). We also find another stable termination in this potential window where every second $-H_2O$ on the CUS site is deprotonated (H_2O/OH) and the bridging oxygen is protonated as seen in Fig. 3. However, our CTR data shows a significant change in the Ru_{CUS}–O bond length between 0.5 V_{RHE} and 1.0 V_{RHE} (Fig. 2D, E, Fig. S12A and B, ESI†) and thus we rule out this structure as a stable surface termination. This could be the intermediate transition between the most stable structures observed at 0.5 V_{RHE} and 1.0 V_{RHE} (blue and green lines respectively in Fig. 3), where the transition from this structure to the stoichiometric surface at $\sim$0.7 $V_{DFT-RHE}$ is in better agreement with the redox peak at $\sim$0.7 V_{RHE}. The computed Ru_{CUS}–O distance associated with water adsorption is much shorter than the experimental value. This shorter Ru_{CUS}–O distance from DFT, and the presence of internal hydrogen bonds as indicated by the observation that water adsorbed at the CUS site donates, rather than accepts, a hydrogen bond to the hydrogen adsorbed on the neighboring bridging oxygen, may result from the absence of hydrogen bonding in the aqueous environment and temperature effects[59] (see Fig. S13, ESI† for comparison between experimental and computational bond lengths).

Surface structure at 1.0 V_{RHE}

Increasing the potential from 0.5 to 1.0 V_{RHE}, CTR measurements revealed that the Ru_{CUS}–O bond distance decreased significantly by $\sim$0.5 Å to 2.19(2) Å and the Ru_{BRI}–O bond length was reduced by $\sim$0.2 Å to 1.95(2) Å, as shown in Fig. 2E and Fig. S12B. The fitted Ru_{CUS}–O bond length of 2.19(2) Å is larger than that of the apical Ru–O bond in bulk (1.94 Å)[4] and comparable to the Ru_{BRI}–O bond length found at 0.5 V_{RHE} (Fig. 2D) while the fitted Ru_{BRI}–O bond length of 1.95(2) Å is comparable to previously reported Ru_{BRI}–O bond lengths of a stoichiometric surface (1.93 Å)[26] and the bulk apical Ru–O bond length (1.94 Å).[4] DFT results showed that removal of protons from bridging oxygen, and the dissociation of every second water molecule on the Ru CUS sites with proton transfer to adjacent bridging oxygens occurs at $\sim$0.5 or 0.7 $V_{DFT-RHE}$, as shown in Fig. 2I and 3. The surface structure fitted from CTR measurements at 1.0 V_{RHE} (Fig. 2E) is consistent with the DFT computed structure at 1.0 $V_{DFT-RHE}$, having H_2O/OH (half coverage each) on the Ru CUS sites, with every second bridging oxygen protonated. The experimental value of Ru–O bond length on the Ru CUS (2.19(2) Å) and bridge sites (1.95(2) Å) is in agreement with the average of the computed bond lengths for a (2 × 1) cell, Ru_{CUS}–O bond length of 2.12 Å and Ru_{BRI}–O bond length of 2.01 Å (Fig. 2I), respectively. It should be noted that this surface structure from DFT (Fig. 2I) consists of two energetically degenerate structures predicted by Reuter *et al.* (O_{BRI}/H_2O_{CUS} and OH_{BRI}/OH_{CUS}),[36] which might be attributed to the larger (2 × 1) unit cell used here, allowing for symmetry breaking and lowered Gibbs energy of adsorption. Moreover, such findings are consistent with recent high resolution STM observations combined with DFT, showing that water clusters on Ru CUS sites are stabilized by donating one hydrogen per two water molecules to the adjacent bridge oxygen sites.[41,42] Therefore, the 0.7 V_{RHE} redox peak observed in cyclic voltammetry can be attributed to the deprotonation of every second bridging oxygen accompanied by the dissociation of every second water molecule on the CUS Ru site.

Surface structure at 1.3 V_{RHE}

Further increasing the potential to 1.3 V_{RHE}, CTR measurements showed that the Ru_{CUS}–O bond length was shortened considerably by $\sim$0.12 Å to 2.07(6) Å while the Ru_{BRI}–O bond length was reduced slightly to 1.90(4) Å, as shown in Fig. 2F and Fig. S12C (ESI†). DFT results showed that deprotonation from the stable surface structure at 1.0 $V_{DFT-RHE}$, H_2O/OH on Ru CUS and OH/O on Ru bridge sites could occur at $\sim$1.1 $V_{DFT-RHE}$, yielding –OH on Ru CUS and a deprotonated bridging oxygen, as shown in Fig. 2J and 3. In this computed structure, adsorbed –OH on Ru CUS sites had a Ru_{CUS}–O bond length of 1.94 Å, which is shorter than CTR-fitted Ru_{CUS}–O (2.07(6) Å) at 1.3 V_{RHE}, while the bridging oxygen had a Ru_{BRI}–O of 1.94 Å. Therefore, we further consider a surface structure having H_2O/OH (half coverage each) on Ru CUS and –O on Ru bridge sites, which is slightly more stable (light grey line in Fig. 3). However, since experimentally, we observe a decrease in the Ru_{CUS}–O bond length from 1.0 V_{RHE} to 1.3 V_{RHE} (Fig. 2E, 2F), we propose an oxidized stoichiometric surface, where all the CUS sites are filled with –OH groups (Fig. 3), possibly with some residual CUS $-H_2O$ (light grey line in Fig. 3). Beyond 1.2 $V_{DFT-RHE}$, although DFT predicted that the fully oxidized surface, having –O on Ru CUS and deprotonated bridging oxygen sites (dark grey line in Fig. 3) would be the most stable, other competing structures such as –OH on Ru CUS on an otherwise stoichiometric surface, were predicted computationally to have a small energy difference relative to this structure (Table S7, ESI†). Considering that (1) the experimental Ru_{CUS}–O bond length of 2.07(6) Å from CTR at 1.3 V_{RHE} is much greater than the apical Ru–O bond length in

the bulk (1.94 Å)[4] and surface Ru_{BRI}–O (1.93 Å)[26] and (2) $–OH_{CUS}$ in the DFT structures had an unsaturated hydrogen bond whose stabilization by the aqueous environment was not considered in the DFT here, we thus proposed that the surface structure at 1.3 V_{RHE} consisted of –OH on Ru CUS and deprotonated bridging oxygen sites. This structure might be stable for the whole voltage range of the fully oxidized structure predicted by DFT. Thus, the 1.1 V_{RHE} redox peak can be attributed to the deprotonation of H_2O/OH on Ru CUS and removal of hydrogen adsorbed to every alternate bridging oxygen site yielding –OH (and some residual $–H_2O$) on Ru CUS and –O on Ru bridge.

Surface structure at 1.5 V_{RHE}

Increasing the voltage from 1.3 to 1.5 V_{RHE} gave rise to a pronounced redox peak at ~1.4 V_{RHE} and the onset of the OER at ~1.5 V_{RHE}. CTR measurements revealed that the Ru CUS site had an –OO like species, having a Ru_{CUS}–O bond length of 2.20(2) Å and an O–O distance of 1.25(5) Å (Fig. 2G and Fig. S12D, ESI†), while the bridge oxygen was unchanged from that found at 1.3 V_{RHE} (Ru_{BRI}–O = 1.94 (3) Å), as shown in Fig. 2F and G.

The proposed surface structure with –OO-like species on the Ru CUS site at 1.5 V_{RHE} was supported by our DFT results, as shown in Fig. 2K and 3. With increasing potential from 1.3 V_{RHE}, the –OH on the CUS site is oxidized to form –O, followed by a second water dissociation on the fully oxidized surface resulting in –OOH on the CUS site. While –OOH groups on the Ru_{CUS} site were unstable, the proton of the –OOH group could be transferred to the neighboring oxygen atom on either the bridge (red line in Fig. 3) or CUS (pink line in Fig. 3) site, with these two states being energetically degenerate, where the transferred proton stabilized the –OO group *via* a hydrogen bond (Table S7, ESI†). A similarly stabilized –OO group was reported recently for the OER on IrO_2(110).[44] Therefore, our combined CTR and DFT results suggested that the Ru CUS sites were filled by –OO species (half coverage) stabilized by a hydrogen bond with –OH (half coverage) present on neighboring Ru CUS or Ru bridge sites, where the remaining Ru bridge or CUS sites were filled with –O.

OER mechanism

In light of these CTR and DFT results in Fig. 2 and 3, we propose a modified OER mechanism for the RuO_2(110) surface from the conventional OER mechanism,[37,39,43] which involves four proton concerted electron transfer steps on the Ru CUS site with the formation of –OH, –O, and –OOH intermediates. The rate-limiting step from –O to –OOH found in the conventional OER mechanism suggests that –OO-like species should not be stable on the surface,[37,39,43] which is inconsistent with our CTR measurements. The modified OER mechanism involves six steps, transferring four protons and electrons concertedly until the final oxygen release, as shown in Fig. 4 (Fig. S16 and S17, ESI†). At 1.5 $V_{DFT-RHE}$, we started with a single empty Ru_{CUS} site on an otherwise fully oxidized surface (I) following the release of the first –OO group from the structure present at 1.5 $V_{DFT-RHE}$. The vacant site was then filled by chemisorbed water (II), which was deprotonated in two subsequent steps to form a fully oxidized surface (IV). Following this step, we propose the adsorption and deprotonation of an additional water molecule to form a precursor state of an –OOH group on the oxygen adsorbed on the Ru_{CUS} site (V), which was immediately followed by the proton transfer step, resulting in a hydrogen-bond-stabilized –OO group on the Ru_{CUS} site (VI). Lastly, the removal of the final proton destabilized the –OO group, leading to the release of oxygen gas (VII). It should be noted that a structure with alternating –OO and –O on the CUS site and a fully oxidized bridge site was found to be ~0.1 eV more stable than state VI (observed in the CTR data) at OER potentials (Fig. S14, ESI†). This small energetic difference of ~0.1 eV falls within DFT uncertainty associated with the specific choice of (PBE-GGA) exchange

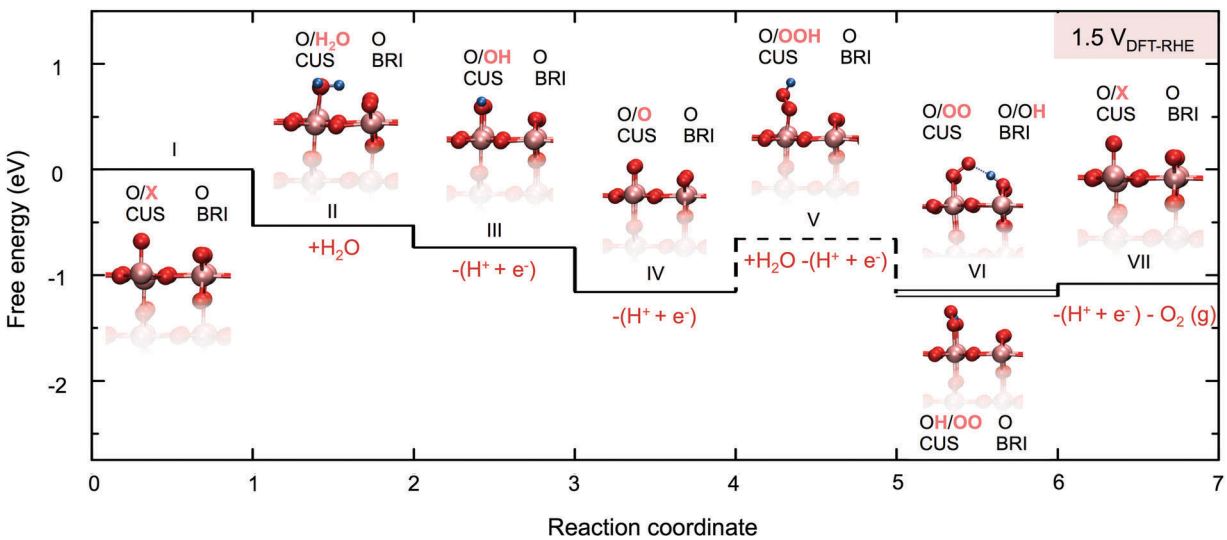

Fig. 4 Free energy diagram at 1.5 $V_{DFT-RHE}$ for the OER mechanism based on DFT calculations showing the six possible intermediates. The dashed line indicates an unstable and an –OOH precursor state, which is needed for –OO formation. Fig. S16 and S17 (ESI†) show the free energy diagram at 0 $V_{DFT-RHE}$ and 1.23 $V_{DFT-RHE}$ respectively. For each intermediate, a ball and stick model of the surface adsorbate configuration is shown. Pink, red and blue spheres represent Ru, O and H atoms respectively. Hydrogen bonds are drawn with blue dashed lines where applicable.

correlation functional to study OER intermediates[60] and the lack of explicit water in the calculations (Fig. S15, ESI†). In this modified OER mechanism, the last step (VII) from deprotonating –OH present on neighboring Ru CUS or Ru bridge sites and simultaneous molecular oxygen release from the Ru CUS sites is considered rate-limiting for the OER. Recent DFT studies on IrO_2 show that the transformation of –OOH to molecular oxygen is not completely downhill in free energy. Instead, the barrierless transformation of –OOH to an –OO structure can be stabilized by a neighboring –OH group. However, even with the stabilization effect, the rate limiting step for IrO_2(110) was found to be the dissociation of the second water molecule. Through our studies on RuO_2(110), we experimentally and theoretically determine the presence of a similar –OOH stabilized structure and suggest that the removal of the last proton to form oxygen gas is rate limiting. Therefore, evidence from CTR and DFT for the formation of such an –OO intermediate on RuO_2(110) at OER-relevant potentials highlights that adsorption configurations can play a significant role in predicting the OER pathway and add increased complexity to the OER mechanism.

Combined CTR measurements with DFT results confirmed that Ru CUS generates active sites for the OER. With increasing voltage, Ru CUS can be filled gradually from –H_2O, H_2O/OH, and –OH, to OO/OH or O/OO stabilized by neighboring protonated bridging oxygens at OER-relevant potentials. No evidence was found to support lattice oxygen involvement reported previously for RuO_2,[61,62] which is in agreement with recent online electrochemical mass spectrometry (OLEMS) measurements on oriented RuO_2 films and powders,[47] showing no measurable oxygen exchange unlike Co-based perovskites.[63] In addition, having no significant changes for surface Ru positions as a function of potential, and a Ru_{CUS}–O length of 2.20(2) Å and a Ru_{BRI}–O length of 1.94(3) Å at 1.5 V_{RHE} from the CTR measurements does not support the previous proposal of higher valent oxides to form molecular oxygen.[17–19] Although this modified mechanism did not discuss chemical combination of oxygen atoms from two neighboring oxidized Ru sites,[64] this process cannot be excluded at this time and requires further investigation. The binding of oxygenated species on the Ru bridge sites on RuO_2(110) is too strong to generate –OO, which is considered as the surface precursor of molecular oxygen release. Having Ru CUS responsible for generating OER active sites is consistent with previous work that correlates increasing Ru CUS site density on the surface with increasing OER activity.[5,46,47] This work also highlights opportunities for reducing the adsorption strength of oxygenated species on the bridge sites, which are inactive for oxygen evolution.[39]

Conclusions

Our work combines *in situ* surface diffraction measurements with DFT calculations to determine the surface atomic structure changes of single-crystal RuO_2(110) in acid as a function of voltage. The (110) facet exhibits distinct redox features at 0.7, 1.1 and 1.4 V_{RHE}, which can be attributed to different oxygenated adsorbates on Ru CUS and bridge sites while the position of the Ru atoms remain relatively unchanged on the surface. Combined CTR and DFT results indicate that (1) the 0.7 V_{RHE} redox peak can be attributed to deprotonation of –H_2O (or H_2O/OH) on Ru CUS sites and hydrogen adsorbed to bridging oxygen to yield H_2O/OH on Ru CUS with only every second bridging oxygen having adsorbed hydrogen; (2) the 1.1 V_{RHE} redox peak can be attributed to deprotonation of H_2O/OH on Ru CUS and the remaining adsorbed hydrogen on bridging oxygen, yielding –OH on the Ru CUS site of an otherwise stoichiometric surface; (3) the 1.4 V_{RHE} redox peak can be attributed to the formation of –OO groups on the Ru CUS sites stabilized by a hydrogen bond with –OH on neighboring Ru CUS sites or protons adsorbed to neighboring bridging oxygen sites. Moreover, our work confirms that Ru CUS sites are the active sites for the OER on RuO_2(110). The surface atomic structure determined from CTR and DFT at OER-relevant potentials (1.5 V_{RHE}) allows us to propose a modified OER pathway from the conventional mechanism. This modified OER mechanism proceeds *via* a single CUS site pathway, with the first water dissociating to form an –OH species that is eventually deprotonated to form a fully oxidized surface. The second water dissociation results in a stabilized –OO structure, where the –OO group is stabilized by a neighboring –OH. The loss of the final proton from this –OH group leads to the evolution of oxygen.

This work extends the understanding of the fascinating surface chemistry of RuO_2 from the UHV environment to electrochemical systems. *In situ* monitoring of the surface structural changes, and the nature of adsorbed species provides novel and unique insights, which identify the active site and elucidate its role in catalyzing the oxygen evolution reaction on RuO_2(110). This study demonstrates that advances in *in situ* surface scattering techniques, coupled with theoretical calculations, can extend our understanding of surface electrochemical processes beyond traditionally studied noble metal surfaces to metal oxides, where different metal and oxygen sites can play unique roles in electrocatalytic processes. Gaining insight into the structural transitions accompanying redox processes using model single crystal surfaces is a powerful tool that can be used to link adsorption energetics to OER kinetics. While currently employed surface diffraction and theoretical methods are only applicable to model well-defined surfaces, the resultant understanding of active sites and reaction mechanisms paves the way for improved catalyst design by directing the search for active and cost-effective catalysts. Our work then, enables the rational design of OER catalysts, beyond traditionally studied RuO_2, by tuning active site density and adsorption energetics for key intermediates.

Methods

Experimental methods

Electrochemical measurements. Oriented RuO_2(110) crystals were synthesized by oxidative evaporation/redeposition of RuO_2 powders as described in ref. 48 and 54. Electrical contacts were

applied to the back of the RuO_2 single crystal and the crystal was mounted in Teflon (FEP 100, DuPont, Wilmington, DE) with the (110) facet exposed to the electrolyte solution. Electrochemical measurements were performed using a Biologic SP-300 potentiostat in a four-neck glass cell. Around 120 mL of a solution of 0.1 M $HClO_4$ (70% Veritas® double distilled) was prepared using deionized water (Millipore, >18.2 MΩ cm). A 4 M saturared Ag/AgCl reference electrode (Pine) was used and calibrated to the RHE scale in 0.1 M $HClO_4$. A large surface area Pt wire was used as the counter electrode. The pH for each measurement was obtained using a pH meter. The electrolyte was presaturated by bubbling Ar for ~60 minutes and the Ar was left bubbling during the course of the measurement to inhibit oxygen reduction at lower potentials. Cyclic voltammetry scans were performed at a scan rate of 50 mV s^{-1}. Electrical impedance spectroscopy measurements were conducted at the open circuit voltage with an amplitude of 10 mV. The reported potentials were corrected for the electrolyte/cell resistance from the high frequency intercept of the real resistance obtained from the Nyquist plot (~50 Ω). The electronic resistance between the wire and the single crystal surface was ~3 Ω.

X-ray scattering measurements. Synchrotron-based X-ray sources were used to measure both specular as well as off-specular reflectivity data, known as truncation rods. While the specular rods provide information about the electron density normal to the electrode surface, the off-specular rods are used to obtain information about the lateral structure of the electrode–electrolyte interface. Measurements were carried out at 0.5 V, 1.0 V, 1.3 V and 1.5 V_{RHE}. Experimentally, potentials higher than 1.5 V_{RHE} could not be accessed by CTR since the large amount of evolved oxygen interfered with the measurements. The X-ray scattering measurements were performed in the reflection geometry at the Synchrotron Radiation Lightsource (SSRL, BL 7-2) and the Advanced Photon Source (BL 12-ID-D). The (00L), (02L), (20L) and (11L) rods were measured at SSRL and the (01L) and (10L) rods were measured at APS. An X-ray transparent Kapton foil (100 μm) was used as a membrane. It is essential to only have a thin layer of electrolyte trapped between the electrode surface and an X-ray transparent membrane in the reflection geometry.[65] This geometry minimizes the background scattering from the electrolyte and enables the measurement of the extremely low intensity of the oxygen rods. In order to obtain a thin layer without any bubbles, the air from the cell was sucked out using a syringe attached to the electrolyte inlet, while the electrolyte outlet was sealed. After ensuring the cell was completely vacuumed, electrolyte was injected through the syringe, and a thin layer formed between the single crystal and the Kapton foil due to capillary forces. A solution of 0.1 M $HClO_4$ (70% Veritas® double distilled) solution was prepared using deionized water (Millipore, >18.2 MΩ cm). The counter electrode used was a Pt wire, and the reference electrode used was a saturated Ag/AgCl electrode (BAS, West Lafayette, IN).

The cell was mounted on a Huber six-circle (4S + 2D) at SSRL and a Huber four-circle (2S + 2D) at APS. Initial sample alignment was performed using a laser beam to ensure that the sample normal was aligned along the main axis of the diffractometer. The specular rods were recorded using a configuration with the incidence angle = exit angle. For the oxygen rods, the incidence angle was fixed at 2° for lower l values, and at 15° for higher l values of the rod. An orientation matrix was calculated to relate the motor angles to the Miller indices (*hkl*) by locating Bragg reflections from the dry sample. The measurements were performed by polarizing the surface to a constant potential and measuring the X-ray intensity along a crystal truncation rod. The symmetry inequivalent rods that were measured were (00L), (10L), (01L), (02L), (11L) and (20L). The intensities were measured using a pixel array area detector (PILATUS 100 K model). The measured intensity at each value of (*hkl*) was extracted by integrating the photon count of the pixels in the region of interest (ROI) of the image. The intensity was then corrected for the background noise, illuminated sample surface area, electrolyte thickness and a Lorentz factor that depends on the experimental geometry.

A model of a RuO_2(110) surface was created in GenX. The rutile RuO_2 has a unit cell size of 3.11 Å × 6.36 Å × 6.36 Å and space group $P4_2/mnm$. Rutile RuO_2(110) can have three distinct surface terminations,[28,33,34,38] as shown in Fig. S3 (ESI†), (1) Ru–O termination depicting a fully reduced surface, (2) O1 termination where only the bridge oxygen is filled, and (3) O2 termination, where both the bridge and CUS oxygen are filled. The O1 surface has been considered as the reference structure. The simulated model includes four distinct layers. Only Ru and O were considered in these layers as the technique is insensitive to the presence of hydrogen atoms. First, an 'adsorbed' layer was considered, where the position of adsorbed oxygens was allowed to relax in the *z* direction. For the 1.5 V_{RHE} structure, the higher oxygen above the CUS site was allowed to relax in both the *z* and *y* direction. The *x* and *y* positions for CUS and bridge oxygen bound to surface Ru were fixed at the bulk lattice position of the apical and equatorial oxygen respectively. The second layer consists of a 'surface' layer, comprising alternate rows of surface oxygen and ruthenium atoms. For this layer, the positions of all the ruthenium and oxygen atoms were allowed to vary in the *z* direction. The third layer, namely the 'subsurface' layer, includes all atoms in the unit cell just below the surface. For this layer, the lattice constant in the *z* direction and positions of all atoms were allowed to relax, with tighter constraints than the 'adsorbed' and 'surface' layer. The fourth and final layer, 'bulk', consists of the bulk structure, where only the lattice parameter in the *z* direction is allowed to relax. Detailed initial and final atomic positions and constraints are listed in Tables S1–S6 (ESI†). The fitting software GenX uses genetic algorithms to optimize the positions of the atoms to accurately fit the experimentally measured intensity. The atomic structure is determined by fitting 300 symmetrically independent data points for each potential. The height of the adsorbed oxygen above the surface as well as the surface and sub surface atoms were allowed to relax in the *z* direction (see Tables S1–S6, ESI† for detailed fitting parameters and results for all conditions). Although the surface and subsurface atoms were allowed to relax, their fitted positions were in close proximity to the

bulk positions. The fitting was performed based on the minimization of the Figure of Merit (FOM):

$$\mathrm{FOM}_{\log R_1} = \frac{\sum_i \left|\log\left(\sqrt{Y_i}\right) - \log\left(\sqrt{S_i}\right)\right|}{\sum_i \left|\log\left(\sqrt{Y_i}\right)\right|}$$

where Y_i is the experimentally measured intensity for point i and S_i is the corresponding simulated intensity. All six rods were fitted simultaneously, and for all four potentials, a value less than 0.10 was obtained, suggesting a reliable fit. The uncertainties in the atomic positions were obtained by running the fitting process with different randomly generated initial parameters ten times. The four best-fit solutions were then chosen to compute the average position and standard deviation for each parameter value, following the method described in ref. 66.

Computational methods

DFT calculations were performed using the VASP package[67–69] using the PBE functional[70] and PAW projectors.[71,72] The cutoff energy was chosen as 500 eV. A 6 × 6 × 1 Monkhorst–Pack[73] *k*-point sampling for the super cell studied was used. The calculated super cell was a 1 × 2 replication, with 4 Ru–O layers (2 free to relax and 2 fixed), where the replication was performed along the short axis of the cell. This was done to allow for symmetry breaking, as well as other interactions along this axis, which were observed for multiple geometries. The Gibbs free energies were calculated by correcting the DFT energies by ZPE and vibrational entropy.[74] For the surface, the contributions of all atoms beyond the fully reduced surface to the ZPE and vibrational entropy terms were considered. The adsorbed species were referenced to the table values[75] of gas-phase hydrogen and water at the gas–liquid interface at 0.035 bar at 300 K, respectively.[76] The comparison to experimental electrochemistry data was performed using the computational hydrogen electrode (CHE) approach described by Nørskov *et al.*[76] We calculate the gas-phase O_2 reference *via*

$$G_{O_2(g)} = G_{H_2O(g)} - G_{H_2(g)} - \Delta G_{exp}$$

Conflicts of interest

There are no conflicts to declare.

Acknowledgements

We thank María Escudero-Escribano for her help during CTR data collection. This work was supported in part by the Skoltech-MIT Center for Electrochemical Energy and the Cooperative Agreement between the Masdar Institute, Abu Dhabi, UAE and the MIT, Cambridge, MA, USA (02/MI/MIT/CP/11/07633/GEN/G/00). This work was also supported in part by the Velux Foundations through the research center V-Sustain (Grant 9455). The work by H. Y. was supported by the U.S. Department of Energy (DOE), Basic Energy Sciences (BES), Materials Sciences and Engineering Division, and the work by H. Z. and the use of the Advanced Photon Source were supported by DOE, BES, Scientific User Facility Division (SUFD), under Contract No. DE-AC02-06CH11357. The work by A. M. and the use of the Stanford Synchrotron Radiation Lightsource were supported by DOE, BES, SUFD under Contract No. DE-AC02-76SF00515. A. F. P. acknowledges the Danish Ministry for Higher Education and Science for an EliteForsk travel grant and the Strategic Research's project NACORR (12-133817). This work used the Extreme Science and Engineering Discovery Environment (XSEDE), which is supported by National Science Foundation grant number ACI-1548562.[77] I. E. L. S. acknowledges the Peabody Visiting Associate Professorship, awarded by the Department of Mechanical Engineering at Massachusetts Institute of Technology.

Notes and references

1 S. Trasatti, *Electrochim. Acta*, 1984, **29**(11), 1503–1512.
2 Y. Lee, J. Suntivich, K. J. May, E. E. Perry and Y. Shao-Horn, *J. Phys. Chem. Lett.*, 2012, **3**(3), 399–404.
3 L. Giordano, B. Han, M. Risch, W. T. Hong, R. R. Rao, K. A. Stoerzinger and Y. Shao-Horn, *Catal. Today*, 2016, **262**, 2–10.
4 H. Over, *Chem. Rev.*, 2012, **112**(6), 3356–3426.
5 K. A. Stoerzinger, L. Qiao, M. D. Biegalski and Y. Shao-Horn, *J. Phys. Chem. Lett.*, 2014, **5**(10), 1636–1641.
6 S. Cherevko, S. Geiger, O. Kasian, N. Kulyk, J. P. Grote, A. Savan, B. R. Shrestha, S. Merzlikin, B. Breitbach, A. Ludwig and K. J. Mayrhofer, *Catal. Today*, 2016, **262**, 170–180.
7 N. Danilovic, R. Subbaraman, K. C. Chang, S. H. Chang, Y. J. Kang, J. Snyder, A. P. Paulikas, D. Strmcnik, Y. T. Kim, D. Myers, V. R. Stamenkovic and N. M. Markovic, *J. Phys. Lett.*, 2014, **5**(14), 2474–2478.
8 E. A. Paoli, F. Masini, R. Frydendal, D. Deiana, C. Schlaup, M. Malizia, T. W. Hansen, S. Horch, I. E. L. Stephens and I. Chorkendorff, *Chem. Sci.*, 2015, **6**(1), 190–196.
9 H. B. Gray, *Nat. Chem.*, 2009, **1**(1), 7.
10 M. G. Walter, E. L. Warren, J. R. McKone, S. W. Boettcher, Q. Mi, E. A. Santori and N. S. Lewis, *Chem. Rev.*, 2010, **110**(11), 6446–6473.
11 T. R. Cook, D. K. Dogutan, S. Y. Reece, Y. Surendranath, T. S. Teets and D. G. Nocera, *Chem. Rev.*, 2010, **110**(11), 6474–6502.
12 M. W. Kanan and D. G. Nocera, *Science*, 2008, **321**(5892), 1072–1075.
13 A. Marshall, B. Børresen, G. Hagen, M. Tsypkin and R. Tunold, *Energy*, 2007, **32**(4), 431–436.
14 L. Duan, F. Bozoglian, S. Mandal, B. Stewart, T. Privalov, A. Llobet and L. Sun, *Nat. Chem.*, 2012, **4**(5), 418–423.
15 T. Hisatomi, J. Kubota and K. Domen, *Chem. Soc. Rev.*, 2014, **43**(22), 7520–7535.
16 T. Reier, H. N. Nong, D. Teschner, R. Schlögl and P. Strasser, *Adv. Energy Mater.*, 2016, **7**(1), 1601275.
17 M. E. Lyons and L. D. Burke, *J. Chem. Soc., Faraday Trans. 1*, 1987, **83**(2), 299–321.

18 M. E. Lyons and S. Floquet, *Phys. Chem. Chem. Phys.*, 2011, **13**(12), 5314–5335.
19 R. L. Doyle, I. J. Godwin, M. P. Brandon and M. E. Lyons, *Phys. Chem. Chem. Phys.*, 2013, **15**(33), 13737–13783.
20 T. R. Tow and J. P. Zheng, *J. Electrochem. Soc.*, 1998, **145**(1), 49–52.
21 C. C. Hu, W. C. Chen and K. H. Chang, *J. Electrochem. Soc.*, 2004, **151**(2), A281–A290.
22 K. Naoi and P. Simon, *J. Electrochem. Soc.*, 2008, **17**(1), 34–37.
23 W. C. Fang, J. H. Huang, L. C. Chen, Y. L. O. Su and K. H. Chen, *J. Power Sources*, 2006, **160**(2), 1506–1510.
24 K. S. Exner, J. Anton, T. Jacob and H. Over, *Angew. Chem., Int. Ed.*, 2016, **55**(26), 7501–7504.
25 D. Crihan, M. Knapp, S. Zweidinger, E. Lundgren, C. J. Weststrate, J. N. Andersen, A. P. Seitsonen and H. Over, *Angew. Chem., Int. Ed.*, 2008, **47**(11), 2131–2134.
26 H. Over, Y. D. Kim, A. P. Seitsonen, S. Wendt, E. Lundgren, M. Schmid, P. Varga, A. Morgante and G. Ertl, *Science*, 2000, **287**(5457), 1474–1476.
27 H. Over, M. Knapp, E. Lundgren, A. P. Seitsonen, M. Schmid and P. Varga, *ChemPhysChem*, 2004, **5**(2), 167–174.
28 Y. D. Kim, A. P. Seitsonen, S. Wendt, J. Wang, C. Fan, K. Jacobi, H. Over and G. Ertl, *J. Phys. Chem. B*, 2001, **105**(18), 3752–3758.
29 H. Over, A. P. Seitsonen, E. Lundgren, M. Wiklund and J. N. Andersen, *Chem. Phys. Lett.*, 2001, **342**(5), 467–472.
30 H. Madhavaram, H. Idriss, S. Wendt, Y. D. Kim, M. Knapp, H. Over, J. Aßmann, E. Löffler and M. Muhler, *J. Catal.*, 2001, **202**(2), 296–307.
31 Y. Wang, K. Jacobi, W. D. Schöne and G. Ertl, *J. Phys. Chem. B*, 2005, **109**(16), 7883–7893.
32 Y. Wang, K. Jacobi and G. Ertl, *J. Phys. Chem. B*, 2003, **107**(50), 13918–13924.
33 K. Reuter and M. Scheffler, *Phys. Rev. B: Condens. Matter Mater. Phys.*, 2001, **65**(3), 035406.
34 K. Reuter and M. Scheffler, *Surf. Sci.*, 2001, **490**(1), 20–28.
35 A. Lobo and H. Conrad, *Surf. Sci.*, 2003, **523**(3), 279–286.
36 Q. Sun, K. Reuter and M. Scheffler, *Phys. Rev. B: Condens. Matter Mater. Phys.*, 2003, **67**(20), 205424.
37 J. Rossmeisl, Z. W. Qu, H. Zhu, G. J. Kroes and J. K. Nørskov, *J. Electroanal. Chem.*, 2007, **607**(1), 83–89.
38 Y. S. Chu, T. E. Lister, W. G. Cullen, H. You and Z. Nagy, *Phys. Rev. Lett.*, 2001, **86**(15), 3364–3367.
39 N. B. Halck, V. Petrykin, P. Krtil and J. Rossmeisl, *Phys. Chem. Chem. Phys.*, 2014, **16**(27), 13682–13688.
40 J. F. Weaver, *Chem. Rev.*, 2013, **113**(6), 4164–4215.
41 R. Mu, Z. J. Zhao, Z. Dohnálek and J. Gong, *Chem. Soc. Rev.*, 2017, **46**(7), 1785–1806.
42 R. Mu, D. C. Cantu, V. A. Glezakou, I. Lyubinetsky, R. Rousseau and Z. Dohnálek, *J. Phys. Chem. C*, 2015, **119**(41), 23552–23558.
43 I. C. Man, H. Y. Su, F. Calle-Vallejo, H. A. Hansen, J. I. Martínez, N. G. Inoglu, J. Kitchin, T. F. Jaramillo, J. K. Nørskov and J. Rossmeisl, *ChemCatChem*, 2011, **3**(7), 1159–1165.
44 Y. Ping, R. J. Nielsen and W. A. Goddard III, *J. Am. Chem. Soc.*, 2016, **139**(1), 149–155.
45 D. F. Abbott, S. Mukerjee, V. Petrykin, Z. Bastl, N. B. Halck, J. Rossmeisl and P. Krtil, *RSC Adv.*, 2015, **5**(2), 1235–1243.
46 K. A. Stoerzinger, R. R. Rao, X. R. Wang, W. T. Hong, C. M. Rouleau and Y. Shao-Horn, *Chem*, 2017, **2**(5), 668–675.
47 K. A. Stoerzinger, O. Diaz-Morales, M. Kolb, R. R. Rao, R. Frydendal, L. Qiao, X. R. Wang, N. B. Halck, J. Rossmeisl, H. A. Hansen, T. Vegge, I. E. L. Stephens, M. T. M. Koper and Y. Shao-Horn, *ACS Energy Lett.*, 2017, **2**(4), 876–881.
48 T. E. Lister, Y. Chu, W. Cullen, H. You, R. M. Yonco, J. F. Mitchell and Z. Nagy, *J. Electroanal. Chem.*, 2002, **524**, 201–218.
49 D. Y. Kuo, J. K. Kawasaki, J. N. Nelson, J. Kloppenburg, G. Hautier, K. M. Shen, D. G. Schlom and J. Suntivich, *J. Am. Chem. Soc.*, 2017, **139**(9), 3473–3479.
50 J. Wang, B. M. Ocko, A. J. Davenport and H. S. Isaacs, *Phys. Rev. B: Condens. Matter Mater. Phys.*, 1992, **46**(16), 10321–10338.
51 Y. Gründer and C. A. Lucas, *Nano Energy*, 2016, **29**, 378–393.
52 Y. Liu, A. Barbour, V. Komanicky and H. You, *J. Phys. Chem. C*, 2016, **120**(29), 16174–16178.
53 M. F. Toney, J. G. Gordon, M. G. Samant, G. L. Borges, O. R. Melroy, L. S. Kau, D. G. Wiesler, D. Yee and L. B. Sorensen, *Phys. Rev. B: Condens. Matter Mater. Phys.*, 1990, **42**(9), 5594.
54 T. E. Lister, Y. V. Tolmachev, Y. Chu, W. G. Cullen, H. You, R. Yonco and Z. Nagy, *J. Electroanal. Chem.*, 2003, **554**, 71–76.
55 H. You, Y. S. Chu, T. E. Lister and Z. Nagy, *Jpn. J. Appl. Phys.*, 1999, **38**(S1), 239–244.
56 P. Fenter and N. C. Sturchio, *Prog. Surf. Sci.*, 2004, **77**(5), 171–258.
57 Z. Zhang, P. Fenter, L. Cheng, N. C. Sturchio, M. J. Bedzyk, M. Předota, A. Bandura, J. D. Kubicki, S. N. Lvov, P. T. Cummings, A. A. Chialvo, M. K. Ridley, P. Bénézeth, L. Anovitz, D. A. Palmer, M. L. Machesky and D. J. Wesolowski, *Langmuir*, 2004, **20**(12), 4954–4969.
58 M. Björck and G. Andersson, *J. Appl. Crystallogr.*, 2007, **40**(6), 1174–1178.
59 M. L. Machesky, M. Predota, D. J. Wesolowski, L. Vlcek, P. T. Cummings, J. Rosenqvist, M. K. Ridley, J. D. Kubicki, A. V. Bandura, N. Kumar and J. O. Sofo, *Langmuir*, 2008, **24**(21), 12331–12339.
60 R. Christensen, H. A. Hansen, C. F. Dickens, J. K. Nørskov and T. Vegge, *J. Phys. Chem. C*, 2016, **120**(43), 24910–24916.
61 M. Wohlfahrt-Mehrens and J. Heitbaum, *J. Electroanal. Chem. Interfacial Electrochem.*, 1987, **237**(2), 251–260.
62 K. Macounova, M. Makarova and P. Krtil, *Electrochem. Commun.*, 2009, **11**(10), 1865–1868.
63 A. Grimaud, O. Diaz-Morales, B. Han, W. T. Hong, Y. L. Lee, L. Giordano, K. A. Stoerzinger, M. T. Koper and Y. Shao-Horn, *Nat. Chem.*, 2017, **9**(5), 457–465.
64 G. Lodi, E. Sivieri, A. De Battisti and S. Trasatti, *J. Appl. Electrochem.*, 1978, **8**(2), 135–143.

65 M. F. Toney, J. G. Gordon, M. G. Samant, G. L. Borges, O. R. Melroy, L. S. Kau, D. G. Wiesler, D. Yee and L. B. Sorensen, *Phys. Rev. B: Condens. Matter Mater. Phys.*, 1990, **42**(9), 5594.
66 T. A. Petach, A. Mehta, R. Marks, B. Johnson, M. F. Toney and D. Goldhaber-Gordon, *ACS Nano*, 2016, **10**(4), 4565–4569.
67 G. Kresse and J. Hafner, *Phys. Rev. B: Condens. Matter Mater. Phys.*, 1993, **47**(1), 558–561.
68 G. Kresse and J. Hafner, *Phys. Rev. B: Condens. Matter Mater. Phys.*, 1994, **49**(20), 14251.
69 G. Kresse and J. Furthmüller, *Comput. Mater. Sci.*, 1996, **6**(1), 15–50.
70 J. P. Perdew, K. Burke and M. Ernzerhof, *Phys. Rev. Lett.*, 1996, **77**(18), 3865.
71 P. E. Blöchl, *Phys. Rev. B: Condens. Matter Mater. Phys.*, 1994, **50**(24), 17953.
72 G. Kresse and D. Joubert, *Phys. Rev. B: Condens. Matter Mater. Phys.*, 1999, **59**(3), 1758.
73 H. J. Monkhorst and J. D. Pack, *Phys. Rev. B: Solid State*, 1976, **13**(12), 5188.
74 D. Loffreda, *Surf. Sci.*, 2006, **600**(10), 2103–2112.
75 M. W. Chase, C. A. Davies, J. R. Downey, D. J. Frurip, R. A. MacDonald and A. N. Syverud, *NIST-JANAF Thermochemical Tables*, American Institute of Physics, 3rd edn, J. Phys. Chem. Ref. Data, 1985, vol. 14(Suppl. 1).
76 J. K. Nørskov, J. Rossmeisl, A. Logadottir, L. Lindqvist, J. R. Kitchin, T. Bligaard and H. Jónsson, *J. Phys. Chem. B*, 2004, **108**(46), 17886–17892.
77 J. Towns, T. Cockerill, M. Dahan, I. Foster, K. Gaither, A. Grimshaw, V. Hazlewood, S. Lathrop, D. Lifka, G. D. Peterson, R. Roskies, J. R. Scott and N. Wilkins-Diehr, *Comput. Sci. Eng.*, 2014, **16**(5), 62–74.